RESEARCH ARTICLE

SFB award

Controlling scaffold conductivity and pore size to direct myogenic cell alignment and differentiation

Ivan M. Basurto[1] | Samir A. Muhammad[1] | Gregg M. Gardner[2] |
George J. Christ[1,3] | Steven R. Caliari[1,2] (ORCID)

[1]Department of Biomedical Engineering, University of Virginia, Charlottesville, Virginia, USA

[2]Department of Chemical Engineering, University of Virginia, Charlottesville, Virginia, USA

[3]Department of Orthopedic Surgery, University of Virginia, Charlottesville, Virginia, USA

Correspondence
Steven R. Caliari, Department of Biomedical Engineering, University of Virginia, Charlottesville, VA, USA.
Email: caliari@virginia.edu

Funding information
National Institute of Arthritis and Musculoskeletal and Skin Diseases, Grant/Award Numbers: R01AR078886, R21AR075181; National Institute of General Medical Sciences, Grant/Award Number: T32GM136615

Abstract

Skeletal muscle's combination of three-dimensional (3D) anisotropy and electrical excitability is critical for enabling normal movement. We previously developed a 3D aligned collagen scaffold incorporating conductive polypyrrole (PPy) particles to recapitulate these key muscle properties and showed that the scaffold facilitated enhanced myotube maturation compared with nonconductive controls. To further optimize this scaffold design, this work assessed the influence of conductive polymer incorporation and scaffold pore architecture on myogenic cell behavior. Conductive PPy and poly(3,4-ethylenedioxythiophene) (PEDOT) particles were synthesized and mixed into a suspension of type I collagen and chondroitin sulfate prior to directional freeze-drying to produce anisotropic scaffolds. Energy dispersive spectroscopy revealed homogenous distribution of conductive PEDOT particles throughout the scaffolds that resulted in a threefold increase in electrical conductivity while supporting similar myoblast metabolic activity compared to nonconductive scaffolds. Control of freezing temperature enabled fabrication of PEDOT-doped scaffolds with a range of pore diameters from 98 to 238 μm. Myoblasts conformed to the anisotropic contact guidance cues independent of pore size to display longitudinal cytoskeletal alignment. The increased specific surface area of the smaller pore scaffolds helped rescue the initial decrease in myoblast metabolic activity observed in larger pore conductive scaffolds while also promoting modestly increased expression levels of the myogenic marker myosin heavy chain (MHC) and gene expression of myoblast determination protein (MyoD). However, cell infiltration to the center of the scaffolds was marginally reduced compared with larger pore variants. Together these data underscore the potential of aligned and PEDOT-doped collagen scaffolds for promoting myogenic cell organization and differentiation.

KEYWORDS
electrically conductive, pore size, scaffold, skeletal muscle

1 | INTRODUCTION

Skeletal muscle is characterized by its highly organized structure that is essential for effective force propagation and locomotion. Aligned myofibers, the basic cellular component of skeletal muscle, are grouped into large muscle fiber bundles called fascicles and ultimately into a complete muscle unit.[1,2] An intricate collagenous extracellular matrix (ECM) mirrors the hierarchical structure of skeletal muscle where individual muscle fibers are surrounded by the endomysium, muscle fascicles (perimysium), and the muscle body (epimysium).[3] Coordinated and efficient muscle contraction is facilitated by innervation of each myofiber by a single motor nerve from the peripheral nervous system.[1,4] Upon receiving an electrical stimulus from the nervous system, the inherent electrical properties of skeletal muscle allow for propagation of an action potential throughout the tissue, resulting in rapid, homogenous contraction of the muscle unit.[5,6] The combination of the electrically responsive nature of muscle and its highly organized structure is critical for effective tissue function.

However, during skeletal muscle injury or trauma both tissue architecture and electrical conductivity can be disrupted, resulting in compromised muscle function. Following most injuries skeletal muscle is able to recover by employing a carefully coordinated inflammatory response.[7] By contrast, in the event of traumatic injuries like volumetric muscle loss a significant portion of tissue is compromised, triggering an aberrant wound healing response characterized by chronic inflammation, fibrosis, and ultimately a loss of muscle mass and function.[8,9] Injuries of this nature usually occur as a result of high energy trauma in military populations but can also result from myopathies and surgical loss.[10] Unfortunately, current approaches to treat traumatic muscle injuries are limited and often result in minimal levels of functional recovery.[11] Engineered biomaterials have emerged as an attractive platform to address this clinical need and support improved regenerative outcomes. These material systems can be designed to provide biophysical signals including topographical features, growth factors, and mechanical cues to direct cell fate.[12–16] Biomaterial porosity has also emerged as a critical regulator of regenerative efficacy with various microporous designs displaying immunomodulatory activity that leads to beneficial wound healing outcomes.[17–19] Despite these advances, many biomaterials fail to recreate key biophysical features of skeletal muscle including the anisotropic organization and electrical excitability that are essential to proper function.

To address current limitations in the field, our group recently developed three-dimensional (3D) electrically conductive and aligned collagen scaffolds for skeletal muscle tissue engineering.[20] The scaffolds are manufactured by directional freeze-drying of a collagen-glycosaminoglycan (CG) suspension resulting in aligned collagen struts reminiscent of healthy skeletal muscle ECM. Unlike conventional hydrogel biomaterials, freeze-dried CG scaffolds contain interconnected networks of macropores (typically ~50–400 μm diameter) enabling robust cell infiltration and acellular clinical application for dermal[17] and peripheral nerve[21] repair. By incorporating electrically conductive polypyrrole (PPy) particles into the CG scaffold we found that mouse myoblast (C2C12) cells exhibited cytoskeletal alignment

and improved myogenic differentiation compared with cells in non-conductive scaffolds. While this work highlighted the potential of conductive scaffolds for skeletal muscle tissue engineering, the influence of scaffold architecture, specifically pore size, on myogenic cell fate remains unclear. Previous work demonstrated the importance of CG scaffold pore size on dictating material surface area and permeability, which in turn affects cell adhesion, proliferation, and phenotype.[22–25] Here, we explore how collagen scaffold biophysical properties, including pore size and electrical conductivity, impact skeletal muscle cell metabolic activity, organization, and maturation.

2 | MATERIALS AND METHODS

2.1 | Polypyrrole and poly (3,4-ethylenedioxythiophene) synthesis

PPy nanoparticles were synthesized as previously described.[20] Briefly, 2 g pyrrole monomer was reacted with 72 mmol $FeCl_3$ using vigorous mixing for 24 h under ambient conditions. The resulting black precipitate was washed repeatedly with water and vacuum filtered until the washings were clear. The PPy powder was then dried overnight and passed through a 325-mesh (45 μm) screen. Fourier-transform infrared (FTIR) spectroscopy was used to assess the chemical structure of the PPy particles (Figure S1).

Poly(3,4-ethylenedioxythiophene) (PEDOT) nanoparticles doped with hyaluronic acid (HA) were synthesized using a previously established protocol.[26] First, 0.01 mol EDOT was added to 50 ml of deionized (DI) water in a round bottom flask and mixed thoroughly. In a separate flask sodium HA (0.05 g, Lifecore, MW ~ 82 kDa) and ammonium persulfate (APS, 0.015 mol) were dissolved in 50 ml of DI water. Oxidative chemical polymerization was initiated by adding the HA/APS solution to EDOT under vigorous mixing for 24 h under ambient conditions. Upon completion of the reaction, the resulting black solution was collected and added to an equal volume of acetone and centrifuged at 5000 rpm for 5 min. Unreacted side products were removed by repeated centrifugation with ethanol and DI water. The precipitate was collected and dried in a 60°C oven before being passed through a 325-mesh (45 μm) screen. FTIR spectroscopy was used to assess the chemical structure of the PEDOT particles (Figure S1).

2.2 | Scaffold fabrication

CG scaffolds were fabricated by homogenizing a suspension of 1 wt % microfibrillar type I collagen from bovine Achilles tendon and 0.133 wt % chondroitin sulfate derived from shark cartilage in 0.05 M acetic acid. The suspension was prepared in a recirculating chiller and stored at 4°C to prevent collagen denaturation. Conductive PPy and PEDOT-doped scaffolds were created by mixing 0.5 wt % PPy and 1 wt % PEDOT nanoparticles, respectively, into the CG suspension via vortexing. All scaffolds were fabricated via directional lyophilization in

which the suspension was loaded into a thermally mismatched mold and freeze-dried using a VirTis Genesis pilot scale freeze-dryer.[20,23] Control of the freezing temperature during lyophilization allowed for user-defined modulation of the resulting scaffold pore size. Scaffolds with variable pore size were fabricated at freezing temperatures of −10, −20, and −55°C (Figure S2). Following lyophilization, all scaffolds were dehydrothermally crosslinked at 105°C for 24 h.

2.3 | Scanning electron microscopy analysis

Scanning electron microscopy (SEM) coupled with energy dispersive spectroscopy (EDS) was used to quantify PPy and PEDOT particle diameter and distribution within the conductive scaffolds. PPy and PEDOT particle size was quantified from three distinct fields of view for a total of 150 particles using ImageJ's measure function. The presence of chlorine was used to track the PPy content due to the use of $FeCl_3$ as a chemical dopant during synthesis as well as its relative scarcity in collagen. Similarly, sulfur elemental mapping was used to detect PEDOT particle distribution because it is a major component of PEDOT's molecular structure and is not abundantly found in collagen. Pore anisotropy was also characterized using SEM of the transverse (orthogonal to freezing direction) and longitudinal (parallel to freezing direction) scaffold planes under low vacuum settings. No coating was applied to scaffolds prior to SEM analysis.

2.4 | Scaffold hydration and crosslinking

Following freeze-drying scaffold cylinders (~15 mm length, 8 mm diameter) were hydrated in 70% ethanol for 30 min before transfer to PBS. The scaffolds were then chemically crosslinked using 1-ethyl-3-(-3-dimethylaminopropyl) carbodiimide hydrochloride (EDC) and N-hydroxysulfosuccinimide (NHS) at a molar ratio of 5:2:1 EDC:NHS:COOH where COOH is the carboxylic acid content of the collagen. CG scaffolds were incubated in sterile-filtered EDC/NHS solution for 50 min under moderate shaking before washing twice with PBS. The scaffolds were then transferred to 70% ethanol to sterilize overnight before washing repeatedly with sterile PBS. All scaffolds were stored at 4°C in sterile PBS until use.

2.5 | Scaffold mechanical characterization

Scaffold compressive mechanical properties were assessed using an TA Instruments Discovery Hybrid Rheometer 3 and a parallel plate geometry (8 mm diameter) following hydration and crosslinking. Scaffolds were tested in longitudinal compression at a strain rate of 0.03 μm/s for a total displacement of 1 mm. Compression tests were chosen for mechanical characterization because collagen scaffolds typically fail in compression.[27] Scaffold elastic modulus was calculated by determining the slope of the linear portion of the stress versus strain curve using a linear regression. All experimental groups were tested in triplicate.

2.6 | Conductivity measurements

To decouple the electrical conductivity imparted by ions in PBS, all scaffolds used to measure conductivity were hydrated in DI water. Collagen scaffolds were loaded into a platinum electrode parallel plate cell and the heights of the probes were adjusted to establish uniform contact. The length (L) of the scaffold was measured as the distance between the probes using digital calipers. Linear sweep voltammetry (LSV) was applied to the parallel plate cell using EC-Lab® software from Biologic Science Instruments. The resistance (R) of the scaffold was calculated using the slope of the linear regression fit to the linear portion of the LSV data (0.5–0.9 V) using Ohm's law. Conductivity (δ) was calculated by Pouillet's law:

$$\delta = \frac{L}{RA},$$

where L is length, A is the surface area of scaffolds, and $A = \pi D^2/4$ where D is the sample diameter.[28] Three scaffolds per experimental group were tested.

2.7 | Cell culture

Immortalized mouse myoblasts (C2C12s) were purchased from ATCC and used at passage 5. C2C12s were cultured in standard tissue culture flasks in growth media: high glucose Dulbecco's Modified Eagle's medium (DMEM), 10 v/v% fetal bovine serum (Gibco), and 1 v/v% penicillin streptomycin (Invitrogen). For differentiation experiments, C2C12s were cultured in media composed of high glucose DMEM supplemented with 2 v/v% horse serum (Gibco) and 1 v/v% penicillin streptomycin. All cultures were performed at 37°C and 5% CO_2.

2.8 | Scaffold culture conditions

C2C12 myoblasts were seeded and cultured within nonconductive as well as conductive CG scaffolds doped with 0.5 wt % PPy or 1 wt % PEDOT. Sterilized scaffold discs (8 mm diameter, ~4 mm thickness) were washed repeatedly with PBS before incubation in growth media for 30 min. Scaffolds were then blotted on a Kimwipe and 10 μl of cell suspension (6.25 × 10⁴ cells) was added to each scaffold and incubated at 37°C for 20 min. Scaffolds were then turned over and seeded with an additional 10 μl of cell suspension for a total of 1.25×10^5 cells per scaffold. Cell-seeded scaffolds were maintained at 37°C and 5% CO_2 in growth or differentiation media that was changed every 3 days for the duration of the experiment. To assess cell differentiation, myoblasts were first cultured in growth media for 3 days before transferring to differentiation media.

2.9 | Quantification of cell metabolic activity

Myoblast cell health within CG scaffolds was assessed using an alamarBlue mitochondrial metabolic activity assay. Cell-seeded scaffolds were incubated in alamarBlue solution for 1.25 h at 37°C with gentle shaking. Following metabolic breakdown of the alamarBlue, the fluorescent byproduct (resorufin) was measured using a Synergy 4 BioTek fluorescence spectrophotometer. The relative cell metabolic activity was calculated by interpolating fluorescence readings using a standard curve derived from known cell numbers. Three scaffolds were tested per experimental group.

2.10 | Scaffold pore size and specific surface area analysis

Scaffold pore size (diameter) was analyzed using confocal microscopy for four different freeze-drying conditions: nonconductive CG scaffolds frozen at −10°C and conductive CG scaffolds incorporating 1 wt % PEDOT frozen at −10, −20, or − 55°C. Scaffolds were stained with a 2 μM solution of AlexaFluor 647 NHS ester in PBS for 20 min under moderate shaking to visualize the pore microstructure. 10 μm thick z-stacks of the transverse and longitudinal cross-sections were imaged using a Leica SP5 confocal microscope. A custom MATLAB program was used to compute the best-fit ellipse representation of the pore shape from the confocal images.[29,30] The pore diameter (d) was calculated based on the values of the major (a) and minor (b) axes of the best-fit ellipse using the following equation[30]:

$$d = \sqrt{\frac{a^2 + b^2}{2}}.$$

Scaffold pore diameter for transverse and longitudinal planes was analyzed for three scaffolds per experimental group.

CG scaffold specific surface area can be calculated by approximating the scaffold pore microstructure as a tetrakaidekahedral unit cell that packs to fill space and minimizes surface energy.[22] Using cellular solids theory of open-cell foams, the specific surface area of CG scaffolds can be approximated using the following equation:

$$\frac{SA}{V} = \frac{0.718}{d},$$

where (SA/V) denotes the specific surface area (surface area/volume).[24]

2.11 | Immunocytochemistry

The collagen backbone was stained with a 2 μM solution of AlexaFluor 647 NHS ester in PBS for 20 min under moderate shaking prior to cell culture. After the culture period, all scaffolds were fixed in 10% formalin and permeabilized with 0.1% Triton X-100 in PBS for 30 min.

Scaffolds were then washed thrice with PBS before additional staining.

The extent of myoblast infiltration into 3D scaffolds was assessed by acquiring tile scan images (5 × 1) of the fluorescently labeled collagen backbone and DAPI-labeled nuclei. Scaffolds were cut in half along the longitudinal plane to image myoblasts in the center of the scaffold discs. The tile scan images were then divided into five zones based on the thickness of the scaffold with zones 1 and 5 defined as the top and bottom of the scaffold discs where cells were originally seeded, zone 3 as the middle of the scaffold disc, and zones 2 and 4 as intermediate between the scaffold periphery and middle. The cell nuclei in each zone were counted using ImageJ's analyze particle tool. The quantified cell number per zone was normalized to the total number of cells within each scaffold and the thickness of each zone.

To visualize the cell cytoskeleton, scaffolds were incubated with fluorescein phalloidin (1:200 dilution) in PBS for 30 min. For primary antibody staining scaffolds were blocked in a 3 wt % BSA in PBS solution for at least 1 h to block nonspecific binding. Scaffolds were then incubated overnight with a myosin heavy chain (MHC) antibody (MF20, mouse monoclonal, eBioscience, 1:200) in 3 wt % BSA solution. Next, samples were washed three times with PBS for 5 min and incubated with AlexaFluor 488-conjugated goat antimouse (1:200) secondary antibody for at least 2 h. Following incubation, scaffolds were washed twice more with PBS and finally the cell nuclei were stained with DAPI (1:1000 dilution) in PBS for 5 min. Samples were stored in PBS at 4°C and protected from light until imaging. Myoblast differentiation was examined by measuring MHC expression via confocal microscopy across three scaffolds per experimental group (nine fields of view).

2.12 | Assessment of scaffold strut and cell alignment

Scaffold anisotropy and cell cytoskeletal alignment were quantified using the "Distribution" function within the OrientationJ plugin for ImageJ. Collagen strut alignment was determined for both the transverse and longitudinal planes using backscattered SEM images. Cytoskeletal alignment was measured using confocal microscopy following 7 days of culture in growth medium. In both cases feature alignment was characterized for three independent scaffolds per experimental group. Feature anisotropy is reported in terms of orientation angle (−90°- +90°) for samples taken from the transverse and longitudinal planes.[23] 0° corresponds to the angle of heat transfer during directional lyophilization in longitudinal sections. For F-actin organization results were normalized to the total amount of F-actin positive pixels in the field of view to account for differences in cell density.

2.13 | RT-qPCR analysis

mRNA was extracted from scaffolds after 9 days of culture in differentiation media using an RNeasy Plant Mini kit following the

manufacturer's instructions. RNA was then reverse transcribed to cDNA using the QuantiTect Reverse Transcription kit at 1 μg per reaction. Quantitative real-time PCR reactions were performed in triplicate using a Step One Plus Real-Time PCR system (Applied Biosystems) and QuantiTect SYBR Green PCR master mix. All primer sequences were derived from an online primer bank and synthesized by Integrated DNA Technologies. Expression of the following markers was quantified: mouse myosin heavy chain 2 (*Myh2*), AAGTGACTGTGAAAACA-GAAGCA and GCAGCCATTTGTAAGGGTTGAC; mouse myogenic differentiation factor 1 (*Myod1*), ATCCGCTACATCGAAGGTCTG and CTCGACACAGCCGCACTCTTC; and mouse glyceraldehyde 3-phosphate dehydrogenase (*Gapdh*), AGGTCGGTGTGAACGGATTTG and TGTAGACCATGTAGTTGAGGTCA. Fold changes in gene expression (normalized to the CG group at day 2) were calculated using the delta–delta Ct method with *Gapdh* as the housekeeping gene.

2.14 | Statistical analysis

All data are presented as means and their standard deviations unless otherwise indicated. Myoblast metabolic activity and percentage of cells per zone were statistically analyzed using a paired two-way analysis of variance (ANOVA). A one-way ANOVA was used for all other statistical tests. Upon finding any statistically significant differences via ANOVA, post hoc multiple comparison tests of parameters of interest were performed using Tukey's HSD. These statistical analyses were conducted using GraphPad Prism 9.0. P-values < .05 were considered statistically significant.

3 | RESULTS AND DISCUSSION

3.1 | PPy and PEDOT particles were successfully synthesized

While our previous work focused on the incorporation of PPy particles to create electrically conductive CG scaffolds,[20] we have since observed decreased cell metabolic activity when culturing lower passage C2C12 mouse myoblasts or human muscle progenitor cells in PPy-doped CG scaffolds compared with nonconductive CG scaffolds. Therefore, we were initially motivated to explore incorporation of alternative conductive polymers that could maintain scaffold electrical conductivity while improving sustained myogenic cell metabolic activity. Numerous electrically responsive polymers have been developed for tissue engineering applications but PPy, polyaniline, and polythiophene polymers such as PEDOT are the most utilized conductive polymers in the biomedical field.[31,32] Furthermore, they are among the few conductive polymers that have been utilized for 3D tissue engineering applications.[31] In particular, PEDOT shows superior electrical conductivity and thermal stability compared with PPy while also lowering its oxidation and reduction potential that could be damaging to cells.[33,34] PEDOT in combination with other materials also supports

cell adhesion, proliferation, and differentiation across numerous electrically responsive cell types.[35–37]

Another key parameter toward the application of conductive polymers is the type of chemical dopant, or charge carrier, used to enable effective propagation of electrical signal. The choice of dopant can have a profound effect on the conductive polymer properties including electrical conductivity as well as structural properties such as porosity, density, roughness, and wettability.[38,39] We hypothesized that the lower levels of cell metabolic activity observed in our PPy-doped scaffolds could be attributed to leaching of the iron (III) chloride (FeCl$_3$) dopant. We therefore chose to use HA as our PEDOT chemical dopant in an effort to improve chemical stability while maintaining high levels of conductivity. An additional advantage of HA is the presence of carboxyl groups that could be chemically crosslinked to the amines in the CG scaffold, thus limiting leaching and improving material stability.

PPy and PEDOT conductive polymers were both synthesized by chemical polymerization. PPy particles were prepared by an oxidation reaction between FeCl$_3$ and pyrrole[40] while PEDOT particles were synthesized by oxidizing EDOT in the presence of HA and APS. Chemical synthesis of both conductive polymers was evaluated using FTIR spectroscopy (Figure S1) and compared with previously published spectra.[26,40,41] For PPy particles, peaks at 1350 and 1220 cm^{-1} were indicative of C–H wagging and C–N in-plane stretching while the peak intensity at 1580 cm^{-1} was associated with C=C stretching that occurs along the π-conjugated polymer backbone.[40,41] For PEDOT the peaks at 1530–1470 cm^{-1} were characteristic of asymmetric stretching of C$_\alpha$=C$_\beta$, while the peaks at 990, 860, and 700 cm^{-1} were attributed to C–S bonds in the thiophene ring.[26] SEM images revealed homogeneous PPy and PEDOT particles with an average diameter of 0.52 ± 0.08 and 2.73 ± 0.44 μm, respectively. This dissimilarity in particle size is likely due to the larger the molecular structure of EDOT and its chemical dopant, HA, as compared with the iron chloride-doped pyrrole particles.

3.2 | PPy and PEDOT particles were uniformly distributed throughout CG scaffolds

Nonconductive CG scaffolds were fabricated by first homogenizing microfibrillar type I collagen and chondroitin sulfate in a recirculating chiller. The resulting suspension was directionally freeze-dried using a custom designed, thermally mismatched mold composed of an insulating Teflon block atop a thermally conductive copper plate.[20,23] The discontinuity in thermal properties within the mold directs heat transfer during the freezing process through the conductive copper, resulting in elongation of the ice crystals in the longitudinal scaffold plane and anisotropy of the collagen struts following sublimation.[23] Electrically conductive CG scaffolds were produced through homogeneous incorporation of either 0.5 wt % PPy or 1 wt % PEDOT particles into the CG suspension prior to directional freeze-drying.

The distribution of conductive particles within lyophilized scaffolds was evaluated using SEM and EDS elemental mapping. Since
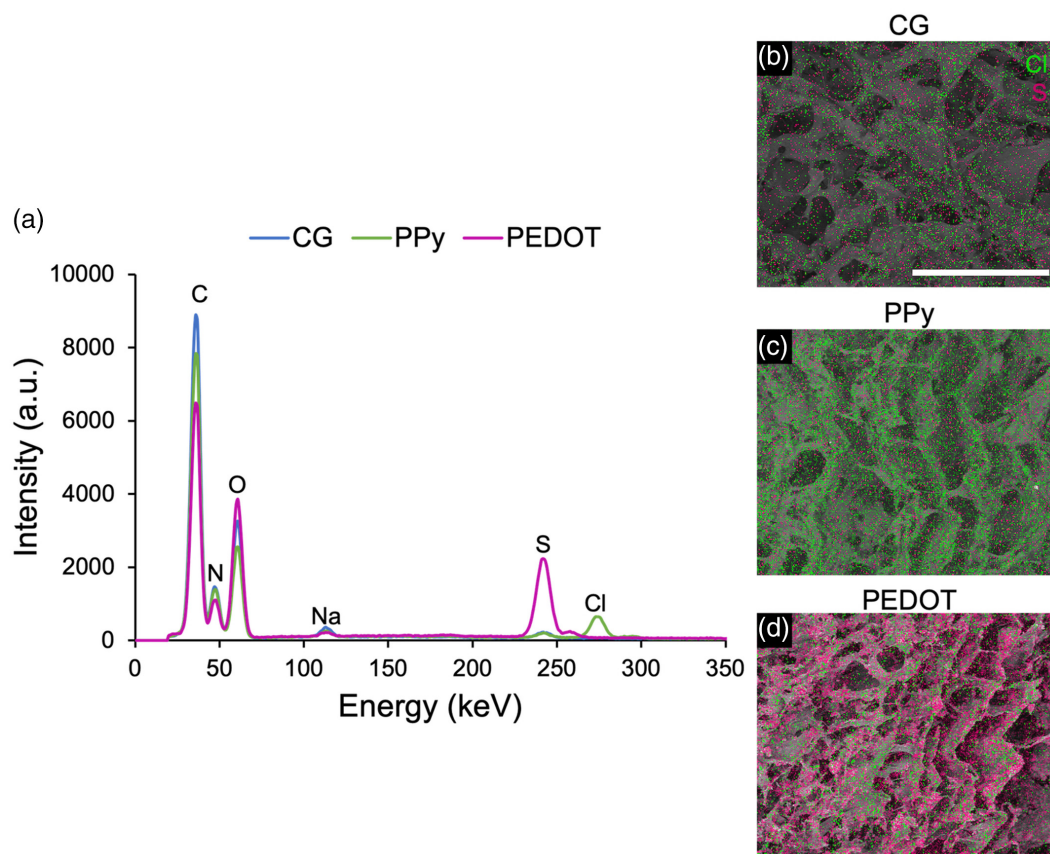
FIGURE 1 EDS mapping revealed uniform conductive polymer distribution throughout CG scaffolds. (A) EDS spectra of the 0.5 wt % PPy and 1 wt % PEDOT-doped CG scaffolds show elemental distributions across experimental groups, including distinct Cl and S peaks with the addition of PPy and PEDOT, respectively. (B–D) EDS maps of Cl (*green*) and S (*pink*) content overlaid on SEM images of longitudinal scaffold planes show homogenous distribution of conductive particles as indicated by the green and pink pixels, respectively, relative to nonconductive CG scaffolds. Scale bar: 300 μm. *n* = 3 scaffolds per experimental group

PPy particles were synthesized using $FeCl_3$ as a chemical dopant, the presence of chlorine (Cl) was used to quantify PPy distribution. Similarly, due to the fact that sulfur (S) is a major component of PEDOT's molecular structure and not abundantly found in collagen, it was used to indicate PEDOT localization with the scaffolds. The EDS spectra showed that there was significantly more Cl and S in PPy and PEDOT-doped CG scaffolds, respectively, compared with nonconductive CG controls (Figure 1). In addition, EDS mapping showed that both PPy and PEDOT were uniformly distributed throughout respective CG scaffolds as indicated by the green and pink pixels denoting Cl and S, respectively.

3.3 | PEDOT-doped CG scaffolds had similar conductivity to PPy-doped scaffolds but supported increased myoblast metabolic activity

Following SEM/EDS characterization to confirm homogeneous conductive particle distribution within CG scaffolds, we next evaluated if the addition of conductive particles improved scaffold electrical properties. Scaffold conductivity was quantified using LSV in a parallel plate cell. LSV has previously been used to evaluate electrical properties in biological sensors and 3D biomaterials by quantifying the current at a reference electrode as voltage is swept linearly with time.[35,42] In addition, LSV allows for rapid and reproducible characterization of scaffold electrical properties regardless of material geometry. By applying a linear regression to the linear portion of the voltage–current curve we were able to calculate scaffold resistance and ultimately conductivity (Figure 2A,B). The addition of 0.5 wt % PPy or 1 wt % PEDOT particles resulted in a threefold increase in scaffold conductivity (2.86 ± 0.93 mS/m, 3.03 ± 0.55 mS/m, respectively) compared with nonconductive CG controls (0.92 ± 0.09 mS/m). These results indicated that conductive polymers were stably incorporated following scaffold hydration and allowed for improved propagation of electrical signals.

While the material conductivity values reported here are modest they fall within the range of previously characterized electrically responsive biomaterials.[32,37,43–45] It is also important to note that we quantified the overall conductivity of the highly porous scaffold (~98%–99% porous), which likely underestimates the electrical properties sensed by cells in direct contact with the solid scaffold material since the scaffold pores are filled with low conductivity fluid. Cellular

FIGURE 2 PEDOT-doped CG scaffolds had similar conductivity to PPy-doped scaffolds but supported increased myoblast metabolic activity. (A) Representative linear sweep voltammetry (LSV) curves of nonconductive CG scaffolds, PPy, and PEDOT-doped scaffolds. (B) The conductivity of CG scaffolds was significantly increased with the addition of both conductive polymers. (C) PEDOT-doped scaffolds supported sustained and increasing myoblast metabolic activity when compared with PPy-doped scaffolds after 7 days of culture. **$p < .01$, ***$p < .001$. $n = 3$ scaffolds per experimental group
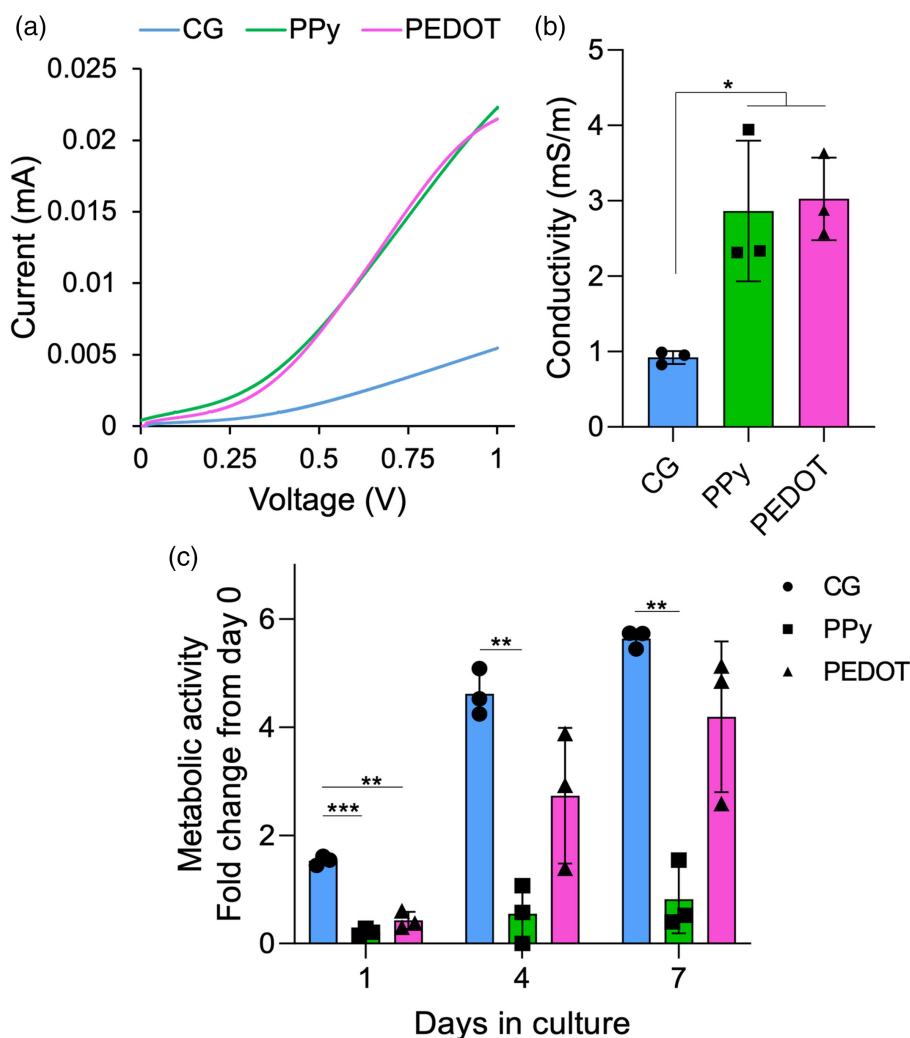
solids theory[46] models the electrical conductivity of open cell foams (δ^*) like CG scaffolds as a function of the relative density, or the volume fraction of solid in the material ($\frac{\rho^*}{\rho_s} \sim 1\%\text{--}2\%$ for our scaffolds based on CG and conductive polymer content), the electrical conductivity of the solid scaffold (δ_s), and the electrical conductivity of the fluid filling the scaffold pores (δ_f, with DI water having conductivity of $\sim 10^{-5}$ S/m[47]):

$$\delta^* = \frac{1}{3}\left[\frac{\rho^*}{\rho_s} + 2\left(\frac{\rho^*}{\rho_s}\right)^{3/2}\right]\delta_s + \left(1 - \frac{\rho^*}{\rho_s}\right)\delta_f.$$

From the above equation we would predict that the solid CG-conductive polymer scaffold content has an electrical conductivity closer to ~ 650 mS/m, or over 200 times greater than the measurements made for the highly porous scaffold composites.

After evaluating scaffold conductivity, mouse myoblast (C2C12) cells were cultured within conductive and nonconductive CG scaffolds over the course of 7 days to evaluate if conductive polymer incorporation impacted cell metabolic activity (Figure 2C). Myoblasts initially showed reduced metabolic activity within conductive scaffolds after the first day of culture compared with nonconductive controls. This is

similar to previously observed results with cell culture in conductive CG scaffolds.[20] We hypothesize the reduced metabolic activity is due to decreased initial cell adhesion resulting from conductive particles blocking cell binding sites present on the collagen backbone. By contrast, following 4 days of culture PEDOT-doped scaffolds supported a marked increase in myoblast metabolic activity that was statistically similar to myoblasts on CG controls. After 7 days of culture PEDOT-doped CG scaffolds continued to facilitate increasing myoblast metabolic activity that was significantly greater than PPy-doped scaffolds.

3.4 | Control of freeze-drying conditions allowed user-defined modulation of scaffold pore size

After exploring how conductive polymer incorporation influenced myoblast metabolic activity, we next aimed to determine how scaffold architecture (pore size) impacted myogenic cell behavior. Previous work clearly illustrated how CG scaffold pore size influences cell adhesion,[23,24,48] differentiation,[48] and response to growth factor stimulation[23] through trade-offs in important scaffold properties. For example, decreasing scaffold pore size increases specific surface
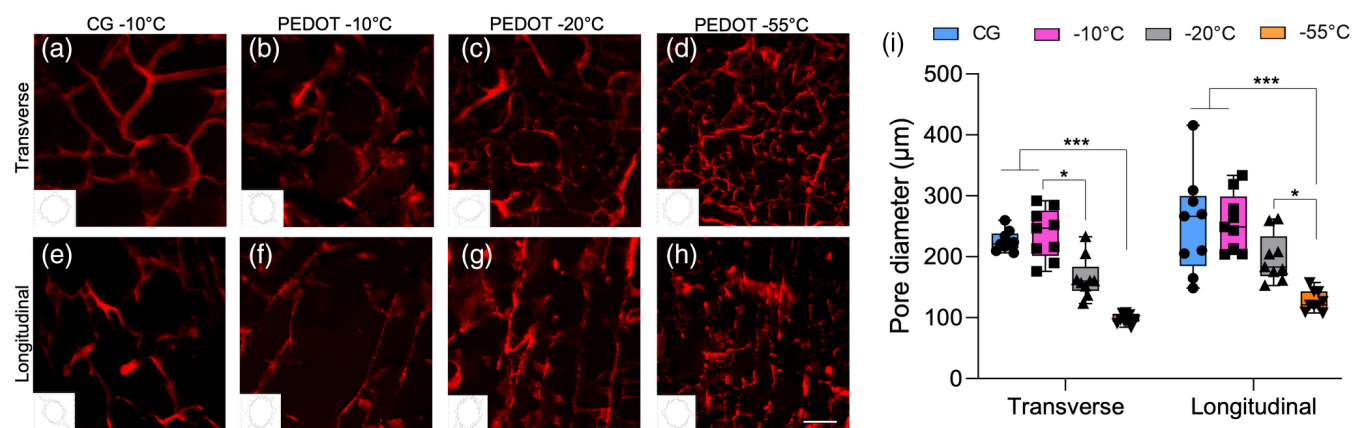
FIGURE 3 Control of freeze-drying conditions allowed for user-defined modulation of scaffold pore architecture. Pore microstructure was evaluated via confocal microscopy of the fluorescently labeled scaffold transverse (A–D) and longitudinal (E–H) planes as a function freezing temperature. Decreasing freezing temperature resulted in scaffolds with smaller pore diameters. *Insets*: best-fit ellipse representations of pore shape generated from MATLAB analysis. (I) Box plot of transverse and longitudinal scaffold pore diameters as a function of freezing temperature. Data presented for each group include the mean (*bar*) while whiskers represent the minimum and maximum. Boxes represent the second and third quartiles. Scale bar: 100 μm. **$p < .01$, ***$p < .001$. $n = 3$ scaffolds per experimental group

TABLE 1 Summary of scaffold material properties as a function of freezing temperature and PEDOT incorporation

	CG (−10°C)	PEDOT (−10°C)	PEDOT (−20°C)	PEDOT (−55°C)
Conductivity (mS/m)	0.92 ± 0.09[a]	3.03 ± 0.55[b]	3.23 ± 0.52[b]	2.73 ± 0.31[b]
Transverse pore size (μm)	226.0 ± 16.7[a,b]	237.5 ± 41.0[a]	165.3 ± 33.7[b,c]	97.9 ± 7.9[c]
Longitudinal pore size (μm)	253.4 ± 82.4[a]	256.6 ± 47.4[a]	198.3 ± 39.4[a]	127.7 ± 16.8[b]
Specific surface area (μm)	0.0032 ± 0.0002[a]	0.0031 ± 0.0006[a]	0.0045 ± 0.0008[b]	0.0074 ± 0.0006[c]

Note: Values are presented as mean ± standard deviation. Statistical differences were analyzed using Tukey's post hoc tests after performing a one-way or two-way ANOVA. Values with the same letter were not significantly different ($p > .05$), while values with dissimilar letters were significantly different ($p < .05$).

area, enabling increased cell adhesion[24] and cell–cell contacts,[23] but simultaneously decreases scaffold permeability.[25] While it is unknown how scaffold pore size influences myogenic cell behavior, optimizing pore architecture is especially critical for skeletal muscle tissue engineering since an idealized scaffold must support robust cell infiltration and multicellular assembly into multinucleated myotubes and myofibers.

Given the capability of PEDOT-doped CG scaffolds to reach equivalent electrical conductivity levels to PPy-doped scaffolds while supporting significantly higher myoblast metabolic activities we focused our remaining experiments with conductive scaffolds on PEDOT-doped materials only. Conductive PEDOT scaffolds with variable pore sizes were fabricated by controlling freeze-drying parameters during directional lyophilization. Specifically, altering freezing temperature enabled user-defined modulation of scaffold pore size. At higher freezing temperatures, ice crystals aggregate in a process known as coarsening to maintain a more thermodynamically favorable state.[22,24] In contrast at lower temperature freezing conditions, nucleation of ice occurs rapidly and remains stable provided the temperature is constant, resulting in the formation of small, discrete ice crystals (Figure S2). Subsequent sublimation

during lyophilization results in a scaffold pore geometry defined by ice crystal size with lower freezing temperatures producing smaller pores.

Nonconductive CG scaffold controls were prepared at a freezing temperature of −10°C while PEDOT-doped constructs were fabricated at freezing temperatures of −10, −20, and −55°C. Scaffolds prepared at −10°C produced the largest average pore diameter as expected, which was not altered by the presence of PEDOT (Figure 3, Table 1). Scaffolds fabricated at −20 and −55°C displayed significantly reduced pore size as freezing temperature decreased. No significant variation in scaffold pore diameter was observed between the longitudinal and transverse scaffold planes. The resultant pore sizes observed were similar to previously published work for nonconductive CG scaffolds fabricated at similar freezing temperatures.[24] Characterization of scaffold mechanical properties showed that neither changes in pore size nor conductivity altered scaffold elastic modulus (Figure S3). While −55°C was the lowest freezing temperature possible with our freeze-drying approach, future work could consider alternative methods to freeze scaffolds at lower temperatures (e.g., in a liquid nitrogen bath) to promote smaller pore size formation.
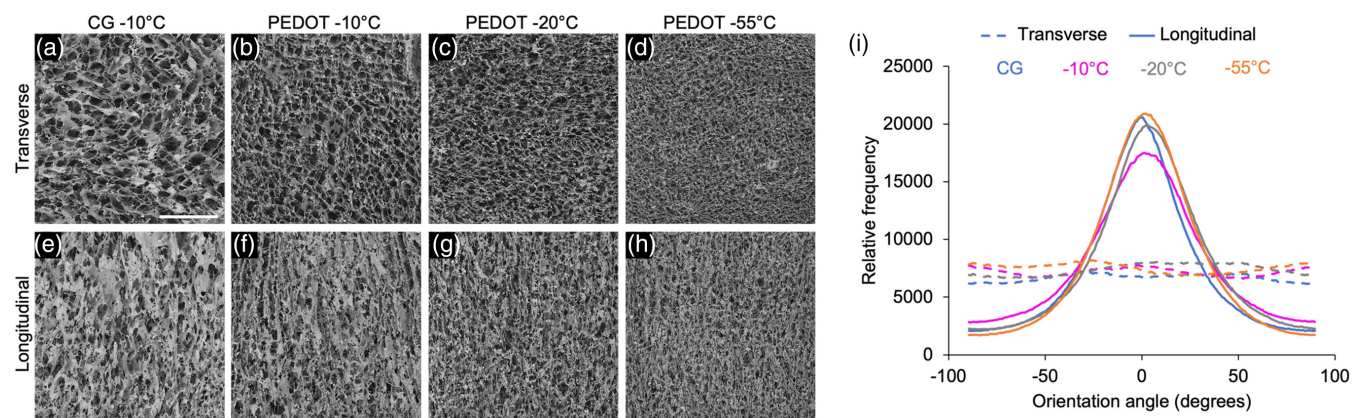
FIGURE 4 Scaffolds showed anisotropically aligned collagen struts independent of PEDOT content and freezing conditions. SEM images (A–D) show a random pore structure along the transverse plane and (E–H) aligned collagen struts in the longitudinal plane that was independent of freeze-drying temperature or addition of conductive particles. (I) Histogram of scaffold strut orientation angles in the transverse (*dashed lines*) and longitudinal (*solid lines*) planes. Scale bar: 300 μm. $n = 3$ scaffolds per experimental group
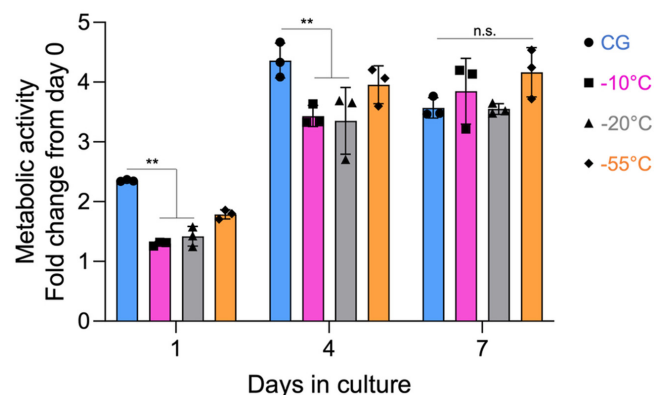

FIGURE 5 PEDOT-doped CG scaffolds supported sustained myoblast metabolic activity independent of pore size. Quantification of metabolic activity after 1 day of culture showed that scaffolds with a larger specific surface area ($-55°C$) allowed for statistically similar levels of cell adhesion following addition of PEDOT compared with nonconductive CG controls. After 7 days of culture PEDOT-doped scaffolds supported sustained myoblast metabolic activity regardless of pore size that was statically similar to nonconductive CG scaffolds. n.s., no significant differences, **$p < .01$. $n = 3$ scaffolds per experimental group

3.5 | Scaffolds showed anisotropically aligned collagen struts regardless of freeze-drying conditions

Given the importance of anisotropic organization on skeletal muscle function, we next assessed if altering freezing temperature and pore size affected the longitudinal alignment of scaffold pores. Scaffold anisotropy was analyzed using SEM images of both the transverse and longitudinal planes. Control of local heat transfer during freeze-drying using a custom designed thermally mismatched mold allowed for alignment of ice crystals prior to lyophilization. Orientation analysis of the scaffolds showed that collagen struts had increased alignment in the longitudinal plane corresponding to the direction of heat

transfer compared with the transverse plane (Figures 4 and S4). Orientation analysis also revealed that the addition of PEDOT particles did not alter collagen strut alignment compared with nonconductive CG scaffolds. Furthermore, scaffold anisotropy proved to be independent of scaffold freezing temperature as indicated by an increased frequency of pore alignment in the direction of heat transfer for all scaffold variants.

3.6 | PEDOT-doped CG scaffolds supported sustained myoblast metabolic activity independent of pore size

Previous work has highlighted the influence biomaterial pore size can have on cell adhesion, proliferation, and differentiation.[23,49,50] To determine if differences in scaffold pore microstructure affected myoblast cell adhesion and metabolic activity, C2C12s were cultured within PEDOT scaffolds fabricated at freezing temperatures of -10, -20, or $-55°C$. Interestingly, PEDOT scaffolds prepared at $-55°C$ supported statistically similar levels of cell metabolic activity compared with nonconductive CG scaffolds (Figure 5) following 1 day of culture. In comparison, -10 and $-20°C$ PEDOT scaffolds supported marked reductions in metabolic activity after 1 day in culture, similar to data shown earlier (Figure 2). This disparity in metabolic activity is likely due to increased initial cell adhesion in scaffolds fabricated at lower freezing temperatures with higher specific surface areas. This is supported by prior work finding that MC3T3-E1 mouse osteogenic cells cultured within CG scaffolds of decreasing pore size (lower freezing temperature, higher specific surface area) also had increased cell attachment.[24] The increased cell adhesion was positively correlated with specific surface area due to the increased availability of cell adhesive ligands.[24] In addition, they found that specific surface area was inversely proportional to pore size, meaning that scaffolds with smaller pores contained greater amounts of available cell adhesive sites. Therefore, the $-55°C$ PEDOT scaffolds possessed a significantly
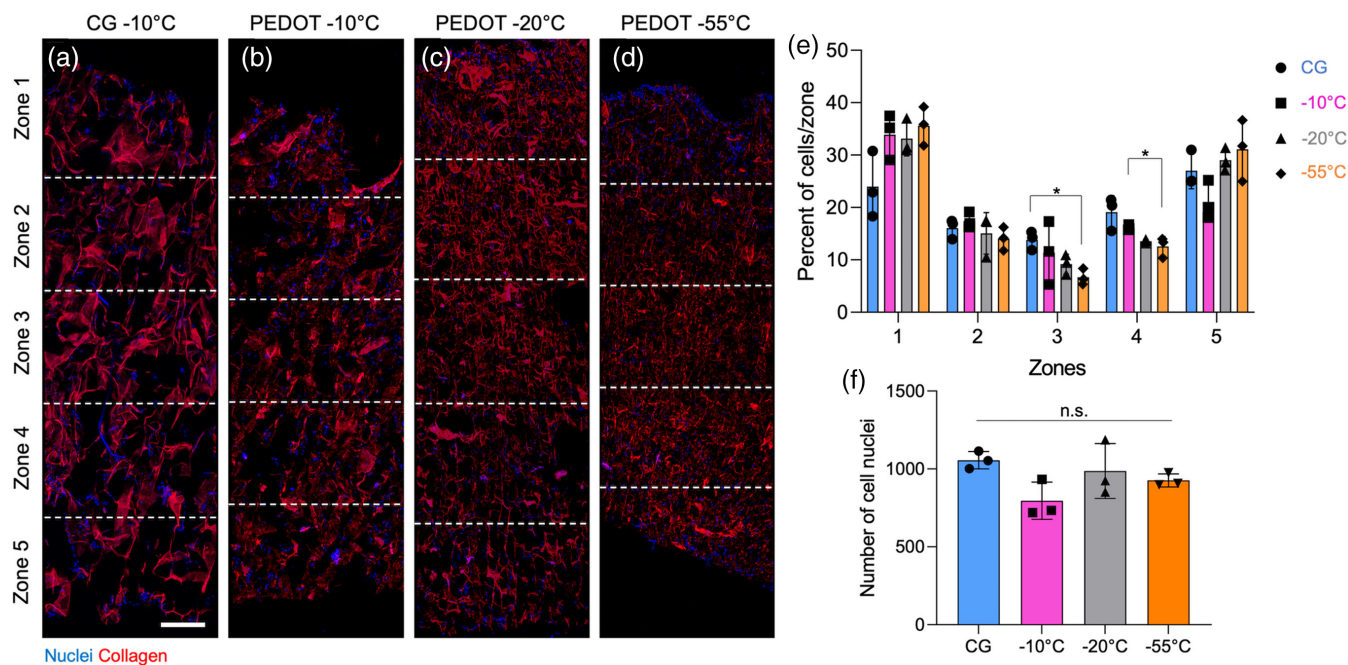
FIGURE 6 Larger pore size allowed marginally improved myoblast infiltration to the middle of the scaffolds. Confocal microscopy images after 7 days of culture showed marginally improved cell penetration to the scaffold center as pore size increased (A–D). Dashed white lines denote scaffold zones where scaffold thickness in the longitudinal plane was divided into fifths (1: *top*, 3: *middle*, and 5: *bottom*) used for cell nuclei quantification. (E) The percentage of cells per zone was highest at the scaffold periphery (zones 1, 5) and decreased toward the center (zones 2–4) as expected based on the cell seeding method. However, scaffolds with larger pore size facilitated significantly increased myogenic cell infiltration as indicated by the greater percentage of cells in middle scaffold zones. (F) Quantification of the total number of nuclei revealed that there were no statistically significant differences between experimental groups. Scale bar: 300 μm. *$p < .05$. $n = 3$ scaffolds per experimental group

greater specific surface area than scaffolds manufactured at other freezing conditions (Table 1). The resulting increase specific surface area and thus ligands for cell binding likely helped rescue cell adhesion in PEDOT-doped CG scaffolds to similar levels observed in nonconductive scaffolds prepared at −10°C following initial cell seeding. Continued culture of myoblasts over the course of 1 week showed that all scaffold groups supported sustained and increasing metabolic activity regardless of pore size or the presence of conductive particles. It is important to note that cell metabolic activity does not necessarily correlate with cell number and is instead an indicator of overall cell health and respiration. Future work could quantify DNA content over time to gain a more complete understanding of cell viability and proliferation in these scaffolds. Overall these results indicate that, while specific surface area is an important factor driving initial cell adhesion, it is not necessarily a critical regulator of sustained cell metabolic activity.

3.7 | Scaffold pore size marginally influences myoblast infiltration

While the data on myoblast metabolic activity provided strong evidence that PEDOT-doped CG scaffolds supported sustained overall myoblast health, we next wanted to obtain a clearer picture of the cell distribution within scaffolds of variable pore size. By dividing images of

the longitudinal scaffold plane into distinct zones we were able to characterize cell infiltration as a function of distance within the scaffold thickness. Confocal microscopy showed that after 7 days of culture higher cell fractions adhered to the scaffold periphery (zones 1, 5) compared with the middle zones regardless of pore size or conductivity (Figure 6). This was unsurprising given that myoblasts were statically seeded on both sides of scaffold discs (8 mm diameter, ~4 mm thickness) as previously described for CG scaffolds.[20,23] However, scaffolds with smaller pore size consistently showed reduced cell fractions in the middle zones with the PEDOT −55°C scaffolds displaying significantly lower cell fractions in zones 3 and 4 compared with larger pore scaffolds. The more uneven 3D cell distribution in smaller pore scaffolds could be due to steric hindrances impeding myoblast migration toward the scaffold center, although it is important to note that even the smallest pore diameter examined (~100 μm) is larger than individual cells and orders of magnitude larger than the nanoscale mesh sizes in conventional hydrogels. The reduced cell infiltration in smaller pore scaffolds could also be attributed to decreased permeability and nutrient transport to the middle of the scaffold. This theory is supported by previous work showing that CG scaffold permeability is inversely proportional to pore size.[25] In addition, quantification of the total number of nuclei throughout the scaffold thickness revealed that there were no statistically significant differences between experimental groups, indicating similar levels of cell proliferation over the 7 day culture. Together, these results indicate that while smaller pore sizes and
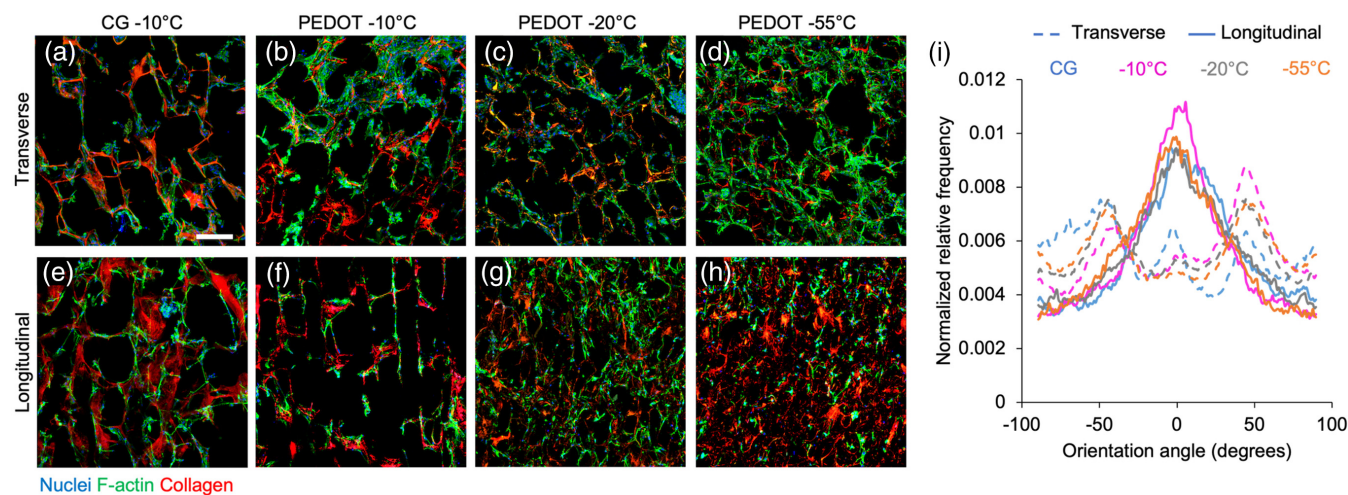
FIGURE 7   Scaffolds guided myoblast cytoskeletal organization independent of conductivity and pore size. Confocal imaging showed that cells organized along the collagen backbone (*red*) and conformed to the contact guidance cues presented. Myoblasts displayed relatively isotropic organization in the transverse planes (A–D) regardless of pore size or addition of PEDOT. Similarly, myoblasts showed modest levels of alignment in the longitudinal planes (E–H) that was independent of scaffold conductivity or pore architecture. (I) Histogram indicating F-actin cytoskeletal alignment in the longitudinal (*solid lines*) versus transverse (*dashed lines*) planes. Scale bar: 100 μm. $n = 3$ scaffolds per experimental group

increased specific surface area allow for improved initial cell adhesion, steric hindrances and/or reductions in permeability and nutrient transport could limit cell infiltration.

3.8 | Myoblasts conformed to contact guidance cues provided by scaffold architecture regardless of conductivity or pore size

After showing that PEDOT-doped scaffolds supported sustained myoblast metabolic activity with cells distributed throughout the 3D scaffold volume, we next analyzed myoblast cytoskeletal organization within all scaffold groups. F-actin cytoskeletal staining revealed that myoblasts organized along the contact guidance cues provided by the scaffold architecture (Figure 7). In addition, similar levels of cell organization and spreading were observed regardless of scaffold pore size or conductivity, indicating that cell organization was governed by scaffold microstructure and geometry. Orientation analysis of F-actin staining showed an isotropic, random alignment of cells in the transverse plane regardless of scaffold group. In addition, a modest level of anisotropic cytoskeletal alignment was observed along the longitudinal plane where collagen struts were aligned in the direction of heat transfer. These results are similar to those observed in prior studies of aligned CG scaffolds and are reminiscent of the high level of organization seen in native skeletal muscle.[20,23]

3.9 | Scaffold pore architecture influenced myogenic differentiation

After evaluating myoblast organization within scaffolds, we finally aimed to characterize the combined influence of electrical conductivity

and pore architecture on myogenic differentiation. Previous work highlighted the importance of CG scaffold architecture on tendon cell phenotype with larger pores leading to enhanced metabolic activity, proliferation, and migration.[23] However, it remains unclear how scaffold pore size impacts myogenic cell phenotype. Analysis of MHC expression, a marker of myogenic differentiation involved in muscle contraction, using confocal microscopy showed no statistical differences in the fraction of cells expressing MHC between experimental groups (Figure 8). Similarly, no differences were observed myoblast fusion index. Interestingly, PEDOT-doped scaffolds prepared at −55°C promoted the greatest area percentage of MHC-positive staining that was statistically greater than the PEDOT-doped −10°C group. RT-PCR further supported these findings showing a significant increase in gene expression of myoblast determination (MyoD), a transcription factor that regulates early myogenesis, in −20 and −55°C scaffolds when compared with scaffolds with larger pore size. These results may indicate that the increased specific surface area present in smaller pore scaffolds is important for enhanced cell adhesion, cell–cell signaling, and subsequent myogenic differentiation. This is corroborated by previous work demonstrating that C2C12 myogenic differentiation is regulated in a density-dependent manner,[51] where myoblasts require contact from sufficient neighboring cells to undergo fusion and maturation.[52] We therefore hypothesize that the smaller pore diameter and increased specific surface area provide by −55°C PEDOT scaffolds allowed for increased cell–cell contacts and myogenesis. Further supporting this hypothesis is that scaffolds fabricated at −10°C (both nonconductive CG and conductive PEDOT) displayed the lowest levels of MHC staining and MyoD gene expression when compared with other experimental groups. These results support the claim that cell–cell contact is a primary driver of 3D myogenic cell differentiation. While it appears that pore size alone has a modest influence on myogenic differentiation, it is clear that additional improvements must be made to
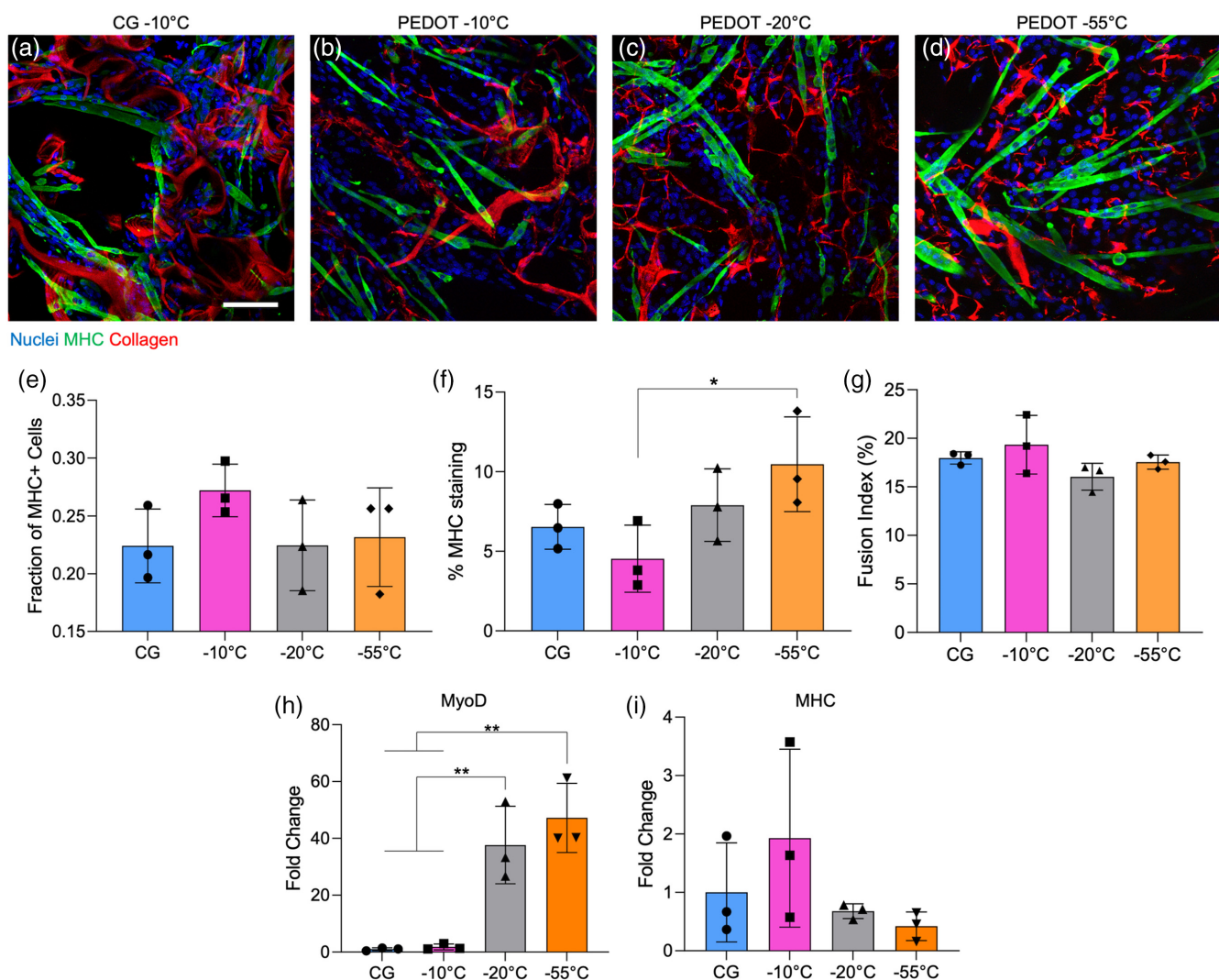
FIGURE 8   Smaller pore conductive scaffolds supported modest increase in MHC staining. Confocal microscopy images showed similar levels of MHC expression following 7 days of culture in differentiation media (A–D). (E) The fraction of MHC-positive cells was consistent across all experimental groups while (F) the area percentage of MHC-positive staining was elevated in smaller pore scaffolds prepared at −55°C. Scale bar: 100 μm. (G) Fusion index, measured as the fraction of MHC⁺ cells incorporated into multinucleated myotubes, showed no statistical difference across experimental groups. (H) qRT-PCR data showed significant upregulation of MyoD in smaller pore scaffold groups (−20, −55°C) compared with larger pore scaffolds. (I) However, there were no statistically significant differences in MHC expression observed. Data are expressed as the mean fold change normalized to expression in the CG group. *$p < .05$, **$p < .01$. $n = 3$ scaffolds per experimental group

create an impactful scaffold design for skeletal muscle tissue engineering. Future work will investigate the influence of mechanical and/or electrical stimulation as well as the source of density of seeded myogenic cells on driving myogenesis.

4 | CONCLUSIONS

In this study, we aimed to explore the combined effects that CG scaffold pore architecture and conductivity have on myogenic cell metabolic activity, alignment, and differentiation. Incorporation of distinct conductive polymers, PPy and PEDOT, into freeze-dried collagen

scaffolds resulted in significantly enhanced electrical properties when compared with nonconductive CG scaffolds. In addition, the inclusion of PEDOT particles facilitated superior metabolic activity compared with PPy-doped scaffolds. To assess if scaffold architecture impacted myogenic cell phenotype, control of freezing temperature during lyophilization allowed modulation of scaffold pore size and specific surface area. PEDOT-doped scaffolds with pore diameters ranging from ~100 to 240 μm were successfully fabricated. Furthermore, directional lyophilization produced a highly organized pore structure that was not altered by the presence of conductive particles or changing of freezing temperature. Scaffolds with smaller pore size and larger specific surface area allowed for improved initial cell adhesion,

higher levels of MHC staining, and increased MyoD gene expression, which is perhaps due to the increased cell–cell contacts facilitated by the scaffold architecture. However, smaller pore sizes also led to marginal reductions in myoblast infiltration toward the center of the scaffolds. Together, these results highlight the utility of PEDOT over PPy for promoting superior myoblast metabolic activity at similar electrical conductivity levels, and that PEDOT-doped CG scaffold pore size can influence initial cell metabolic activity, 3D distribution, and subsequent differentiation.

ACKNOWLEDGMENTS

DATA AVAILABILITY STATEMENT

All data are available from the authors upon reasonable request.

ORCID

Steven R. Caliari https://orcid.org/0000-0002-7506-3079

REFERENCES

1. Musumeci G, Castrogiovanni P, Coleman R, et al. Somitogenesis: from somite to skeletal muscle. *Acta Histochem*. 2015;117:313-328.
2. Nishimura T. Role of extracellular matrix in development of skeletal muscle and postmortem aging of meat. *Meat Sci*. 2015;109:48-55.
3. Gillies AR, Lieber RL. Structure and function of the skeletal muscle extracellular matrix: skeletal muscle ECM. *Muscle Nerve*. 2011;44: 318-331.
4. Gilbert-Honick J, Grayson W. Vascularized and innervated skeletal muscle tissue engineering. *Adv Healthc Mater*. 2020;9:1900626.
5. Sharma KR, Miller RG. Electrical and mechanical properties of skeletal muscle underlying increased fatigue in patients with amyotrophic lateral sclerosis. *Muscle Nerve*. 1996;19:1391-1400.
6. Nicholls JG. The electrical properties of denervated skeletal muscle. *J Physiol*. 1956;131:1-12.
7. Bentzinger CF, Wang YX, Dumont NA, Rudnicki MA. Cellular dynamics in the muscle satellite cell niche. *EMBO Rep*. 2013;14:1062-1072.
8. Corona BT, Rivera JC, Owens JG, Wenke JC, Rathbone CR. Volumetric muscle loss leads to permanent disability following extremity trauma. *J Rehabil Res Dev*. 2015;52:785-792.
9. Ciciliot S, Schiaffino S. Regeneration of mammalian skeletal muscle: basic mechanisms and clinical implications. *Curr Pharm des*. 2010;16:906-914.
10. Initiative, U. S. B. and J. The Burden of Musculoskeletal Diseases in the United States. https://www.boneandjointburden.org/search/node/Muscle (2020).
11. Corona BT, Ward CL, Baker HB, Walters TJ, Christ GJ. Implantation of in vitro tissue engineered muscle repair constructs and bladder acellular matrices partially restore in vivo skeletal muscle function in a rat model of volumetric muscle loss injury. *Tissue Eng Part A*. 2013;20: 131219054609007.
12. Vandenburgh H, Shansky J, Benesch-Lee F, et al. Drug-screening platform based on the contractility of tissue-engineered muscle. *Muscle Nerve*. 2008;37:438-447.
13. Wan AM, Inal S, Williams T, et al. 3D conducting polymer platforms for electrical control of protein conformation and cellular functions. *J Mater Chem B*. 2015;3:5040-5048.
14. Neal D, Sakar MS, Bashir R, Chan V, Asada HH. Mechanical characterization and shape optimization of fascicle-like 3D skeletal muscle tissues contracted with electrical and optical stimuli. *Tissue Eng Part A*. 2015;21:1848-1858.
15. Sanhueza C, Acevedo F, Rocha S, Villegas P, Seeger M, Navia R. Polyhydroxyalkanoates as biomaterial for electrospun scaffolds. *Int J Biol Macromol*. 2019;124:102-110.
16. Chen MC, Sun YC, Chen YH. Electrically conductive nanofibers with highly oriented structures and their potential application in skeletal muscle tissue engineering. *Acta Biomater*. 2013;9:5562-5572.
17. Yannas IV, Lee E, Orgill DP, Skrabut EM, Murphy GF. Synthesis and characterization of a model extracellular matrix that induces partial regeneration of adult mammalian skin. *Proc Natl Acad Sci USA*. 1989; 86:933-937.
18. Bryers JD, Giachelli CM, Ratner BD. Engineering biomaterials to integrate and heal: the biocompatibility paradigm shifts. *Biotechnol Bioeng*. 2012;109:1898-1911.
19. Griffin DR, Weaver WM, Scumpia PO, Di Carlo D, Segura T. Accelerated wound healing by injectable microporous gel scaffolds assembled from annealed building blocks. *Nat Mater*. 2015;14:737-744.
20. Basurto IM, Mora MT, Gardner GM, Christ GJ, Caliari SR. Aligned and electrically conductive 3D collagen scaffolds for skeletal muscle tissue engineering. *Biomater Sci*. 2021;9:4040-4053.
21. Harley BA, Spilker MH, Wu JW, et al. Optimal degradation rate for collagen chambers used for regeneration of peripheral nerves over long gaps. *Cells Tissues Organs*. 2004;176:153-165.
22. Harley BAC, Gibson LJ. In vivo and in vitro applications of collagen-GAG scaffolds. *Chem Eng J*. 2008;137:102-121.
23. Caliari SR, Harley BAC. The effect of anisotropic collagen-GAG scaffolds and growth factor supplementation on tendon cell recruitment, alignment, and metabolic activity. *Biomaterials*. 2011;32:5330-5340.
24. O'Brien FJ, Harley BA, Yannas IV, Gibson LJ. The effect of pore size on cell adhesion in collagen-GAG scaffolds. *Biomaterials*. 2005;26: 433-441.
25. O'Brien FJ, Harley B, Waller MA, Yannas I, Gibson L, Prendergast P. The effect of pore size on permeability and cell attachment in collagen scaffolds for tissue engineering. *Technol Health Care*. 2007;15: 3-17.
26. Wang S, Guan S, Wang J, et al. Fabrication and characterization of conductive poly(3,4-ethylenedioxythiophene) doped with hyaluronic acid/poly(L-lactic acid) composite film for biomedical application. *J Biosci Bioeng*. 2017;123:116-125.
27. Divakar P, Yin K, Wegst UGK. Anisotropic freeze-cast collagen scaffolds for tissue regeneration: how processing conditions affect structure and properties in the dry and fully hydrated states. *J Mech Behav Biomed Mater*. 2019;90:350-364.
28. Tayebi A, Yazdimamaghani M, Walker KJ, et al. 3D conductive nanocomposite scaffold for bone tissue engineering. *Int J Nanomedicine*. 2013;9:167.
29. Gibson LJ, Ashby MF. *Cellular Solids: Structure and Properties*. Cambridge University Press; 1997. doi:10.1017/CBO9781139878326
30. Weisgerber DW, Erning K, Flanagan CL, Hollister SJ, Harley BAC. Evaluation of multi-scale mineralized collagen – polycaprolactone composites for bone tissue engineering. *J Mech Behav Biomed Mater*. 2016;61:318-327.

31. Alegret N, Dominguez-Alfaro A, Mecerreyes D. 3D scaffolds based on conductive polymers for biomedical applications. *Biomacromolecules*. 2019;20:73-89.

32. Guo B, Ma PX. Conducting polymers for tissue engineering. *Biomacromolecules*. 2018;19:1764-1782.

33. Thomas CA, Zong K, Schottland P, Reynolds JR. Poly(3,-4-alkylenedioxypyrrole)s as highly stable aqueous-compatible conducting polymers with biomedical implications. *Adv Mater*. 2000;12: 222-225.

34. Peramo A, Urbanchek MG, Spanninga SA, Povlich LK, Cederna P, Martin DC. In situ polymerization of a conductive polymer in acellular muscle tissue constructs. *Tissue Eng Part A*. 2008;14:423-432.

35. Solazzo M, Monaghan MG. Structural crystallisation of crosslinked 3D PEDOT:PSS anisotropic porous biomaterials to generate highly conductive platforms for tissue engineering applications. *Biomater Sci*. 2021;9:4317-4328.

36. Wang S, Guan S, Xu J, et al. Neural stem cell proliferation and differentiation in the conductive PEDOT-HA/Cs/Gel scaffold for neural tissue engineering. *Biomater Sci*. 2017;5:2024-2034.

37. Yazdimamaghani M, Razavi M, Mozafari M, Vashaee D, Kotturi H, Tayebi L. Biomineralization and biocompatibility studies of bone conductive scaffolds containing poly(3,4-ethylenedioxythiophene):poly(4-styrene sulfonate) (PEDOT:PSS). *J Mater Sci Mater Med*. 2015; 26:274.

38. Balint R, Cassidy NJ, Cartmell SH. Conductive polymers: towards a smart biomaterial for tissue engineering. *Acta Biomater*. 2014;10: 2341-2353.

39. Ravichandran R, Sundarrajan S, Venugopal JR, Mukherjee S, Ramakrishna S. Applications of conducting polymers and their issues in biomedical engineering. *J R Soc Interface*. 2010;7:S559-S579.

40. Lee J, Serna F, Nickels J, Schmidt CE. Carboxylic acid-functionalized conductive polypyrrole as a bioactive platform for cell adhesion. *Biomacromolecules*. 2006;7:1692-1695. doi:10.1021/bm060220q

41. Fu Y, Su Y-S, Manthiram A. Sulfur-polypyrrole composite cathodes for lithium-sulfur batteries. *J Electrochem Soc*. 2012;159:A1420-A1424.

42. Shahrokhian S, Ghalkhani M, Adeli M, Amini MK. Multi-walled carbon nanotubes with immobilised cobalt nanoparticle for modification of glassy carbon electrode: application to sensitive voltammetric determination of thioridazine. *Biosens Bioelectron*. 2009;24:3235-3241.

43. Zhang J, Li M, Kang E-T, Neoh KG. Electrical stimulation of adipose-derived mesenchymal stem cells in conductive scaffolds and the roles of voltage-gated ion channels. *Acta Biomater*. 2016;32:46-56.

44. Severt SY, Ostrovsky-Snider NA, Leger JM, Murphy AR. Versatile method for producing 2D and 3D conductive biomaterial composites using sequential chemical and electrochemical polymerization. *ACS Appl Mater Interfaces*. 2015;7:25281-25288.

45. Vandghanooni S, Eskandani M. Natural polypeptides-based electrically conductive biomaterials for tissue engineering. *Int J Biol Macromol*. 2020;147:706-733.

46. Ashby MF. The properties of foams and lattices. *Philos Trans R Soc Math Phys Eng Sci*. 2006;364:15-30.

47. Pashley RM, Rzechowicz M, Pashley LR, Francis MJ. De-gassed water is a better cleaning agent. *J Phys Chem B*. 2005;109:1231-1238.

48. Murphy CM, Haugh MG, O'Brien FJ. The effect of mean pore size on cell attachment, proliferation and migration in collagen–glycosam inoglycan scaffolds for bone tissue engineering. *Biomaterials*. 2010;31: 461-466.

49. Ferlin KM, Prendergast ME, Miller ML, Kaplan DS, Fisher JP. Influence of 3D printed porous architecture on mesenchymal stem cell enrichment and differentiation. *Acta Biomater*. 2016;32:161-169.

50. Mehr NG, Li X, Chen G, Favis BD, Hoemann CD. Pore size and LbL chitosan coating influence mesenchymal stem cell in vitro fibrosis and biomineralization in 3D porous poly(epsilon-caprolactone) scaffolds: BIOMINERALIZATION IN CHITOSAN-COATED 3D PCL. *J Biomed Mater Res A*. 2015;103:2449-2459.

51. Tanaka K, Sato K, Yoshida T, et al. Evidence for cell density affecting C2C12 myogenesis: possible regulation of myogenesis by cell-cell communication. *Muscle Nerve*. 2011;44:968-977.

52. Gurdon JB, Lemaire P, Kato K. Community effects and related phenomena in development. *Cell*. 1993;75:831-834.

SUPPORTING INFORMATION

Additional supporting information can be found online in the Supporting Information section at the end of this article.